



Stable iridium dinuclear heterogeneous catalysts supported on metal-oxide substrate for solar water oxidation

Yanyan Zhao^{a,1}, Ke R. Yang^{b,1}, Zechao Wang^{c,d,2}, Xingxu Yan^{e,f,g,2}, Sufeng Cao^{h,2}, Yifan Ye^{i,2}, Qi Dong^a, Xizi Zhang^a, James E. Thorne^a, Lei Jin^c, Kelly L. Materna^b, Antonios Trimpalis^h, Hongye Bai^a, Sirine C. Fakraⁱ, Xiaoyan Zhong^d, Peng Wang^{e,f}, Xiaoqing Pan^{g,j}, Jinghua Guoⁱ, Maria Flytzani-Stephanopoulos^h, Gary W. Brudvig^{b,3}, Victor S. Batista^{b,3}, and Dunwei Wang^{a,3}

^aDepartment of Chemistry, Merkert Chemistry Center, Boston College, Chestnut Hill, MA 02467; ^bDepartment of Chemistry, Yale Energy Sciences Institute, Yale University, New Haven, CT 06520; ^cErnst Ruska-Centre for Microscopy and Spectroscopy with Electrons, Forschungszentrum Jülich GmbH, 52425 Jülich, Germany; ^dNational Center for Electron Microscopy in Beijing, School of Materials Science and Engineering, Tsinghua University, 100084 Beijing, China; ^eNational Laboratory of Solid State Microstructures, College of Engineering and Applied Sciences, Nanjing University, 210093 Nanjing, China; ^fCollaborative Innovation Center of Advanced Microstructures, Nanjing University, 210093 Nanjing, China; ^gDepartment of Chemical Engineering and Materials Science, University of California, Irvine, CA 92697; ^hDepartment of Chemical and Biological Engineering, Tufts University, Medford, MA 02155; ⁱAdvanced Light Source, Lawrence Berkeley National Laboratory, Berkeley, CA 94720; and ^jDepartment of Physics and Astronomy, University of California, Irvine, CA 92697

Edited by Alexis T. Bell, University of California, Berkeley, CA, and approved February 13, 2018 (received for review December 20, 2017)

Atomically dispersed catalysts refer to substrate-supported heterogeneous catalysts featuring one or a few active metal atoms that are separated from one another. They represent an important class of materials ranging from single-atom catalysts (SACs) and nanoparticles (NPs). While SACs and NPs have been extensively reported, catalysts featuring a few atoms with well-defined structures are poorly studied. The difficulty in synthesizing such structures has been a critical challenge. Here we report a facile photochemical method that produces catalytic centers consisting of two Ir metal cations, bridged by O and stably bound to a support. Direct evidence unambiguously supporting the dinuclear nature of the catalysts anchored on α -Fe₂O₃ is obtained by aberration-corrected scanning transmission electron microscopy (AC-STEM). Experimental and computational results further reveal that the threefold hollow binding sites on the OH-terminated surface of α -Fe₂O₃ anchor the catalysts to provide outstanding stability against detachment or aggregation. The resulting catalysts exhibit high activities toward H₂O photooxidation.

catalyst | water splitting | solar energy | STEM | spectroscopy

Atomically dispersed catalysts have recently gained significant attention for their advantages of high atomic efficiency, activity, and selectivity (1, 2). Different from bulk heterogeneous catalysts, the atomically dispersed ones feature well-defined structural moieties at the atomic level (3). This feature opens a window to understand mechanisms that underpin heterogeneous catalysts in a similar fashion to how homogeneous catalysts are studied (4). It also presents opportunities to tailor the functionalities of heterogeneous catalysts with unprecedented controls (5). New and unique reaction pathways have been discovered on these catalysts. For instance, when used for CO oxidation, a Pt single-atom catalyst (SAC) has been shown far less susceptible to poisoning by CO than Pt nanoparticles (2). Within this context, research on SACs has thrived, where significant progress in synthesis, characterization, and mechanistic understanding has been made. Notwithstanding, these prior efforts primarily focused on reactions that may require only a single metal-active site, such as CO oxidation (6) and water-gas shift (4). Atomically dispersed catalysts featuring more than one metal-active site are rare in the literature. Consequently, reactions dependent on multiple metal-active sites without organic ligands remain poorly studied. Pioneering works by Iwasawa and coworkers (7) and Gates and coworkers (8, 9) have demonstrated several systems featuring multiple metal atoms per active site for hydroformylation and hydrogenation reactions. Another class of catalysts featuring such structures is found in dinuclear Cu or Ni catalyst for

methane oxidation reactions (10, 11). However, two key challenges remain in this field: (i) to prepare the dinuclear catalyst with a high yield by a facile and general approach and (ii) to achieve a direct observation to unambiguously support the dinuclear nature. To fill in this important knowledge gap, here we report the synthesis of dinuclear heterogeneous catalysts (DHCs) consisting of two Ir atoms per catalytic site stably bound to a support. The structure was enabled by a heterogenization method followed by a room-temperature photochemical ligand removal treatment. The resulting DHCs exhibit outstanding stability against detachment and aggregation yet are highly active toward water oxidation.

Water oxidation was chosen for this present work because, as an essential step in natural and artificial photosynthesis, it has

Significance

While research on single-atom catalysts (SACs) is arguably mature, rare work has been done on atomically dispersed catalyst featuring two atoms. We synthesized Ir dinuclear heterogeneous catalyst in a facile photochemical way. It exhibits outstanding stability and high activity toward water oxidation. The significance of this work can also be appreciated from the catalysis perspective. A grand challenge in heterogeneous catalysis is how to understand the detailed mechanisms at the molecular level, because the most active heterogeneous catalysts are often poorly defined in their atomic structures. Our finding is built upon recent advances aimed at studying SACs but takes a crucial step forward. It provides a material platform to study reactions that would require more than one active site.

Author contributions: Y.Z. and D.W. designed research; Y.Z., K.R.Y., Z.W., X.Y., S.C., Y.Y., Q.D., X. Zhang, J.E.T., L.J., K.L.M., A.T., H.B., S.C.F., X. Zhong, P.W., X.P., J.G., M.F.-S., G.W.B., and V.S.B. performed research; X.Z., P.W., and X.P. supervised the HAADF-STEM efforts; M.F.-S. supervised DRIFTS experiments; Y.Z., K.R.Y., Z.W., X.Y., L.J., X.P., J.G., M.F.-S., G.W.B., V.S.B., and D.W. analyzed data; and Y.Z. and D.W. wrote the paper with comments from all authors.

The authors declare no conflict of interest.

This article is a PNAS Direct Submission.

Published under the PNAS license.

¹Y.Z. and K.R.Y. contributed equally to this work.

²Z.W., X.Y., S.C., and Y.Y. contributed equally to this work.

³To whom correspondence may be addressed. Email: gary.brudvig@yale.edu, victor.batista@yale.edu, or dwang@bc.edu.

This article contains supporting information online at www.pnas.org/lookup/suppl/doi:10.1073/pnas.1722137115/-DCSupplemental.

Published online March 5, 2018.

been a topic of intense research (12). A large number of catalysts have been extensively studied, and their performance has been benchmarked (13). Despite these successes, gaps in the understanding of catalytic water oxidation exist (14). For instance, the mechanisms of heterogeneous catalysts for water oxidation, especially at the molecular level, are poorly understood (15). An important reason has been that the high-performance heterogeneous catalysts are often poorly defined in their structures, especially at the molecular and atomic levels. Despite recent successes in this area (16), the complex interactions between water-oxidation catalysts and light absorbers for integrated solar-to-fuel conversion are still poorly understood (17). Controlled synthesis of high-performance heterogeneous catalysts with well-defined structures and integration with light absorbers are therefore of great importance. Taking an important step aimed at addressing these issues, here we report a facile method for direct synthesis of heterogeneous catalysts consisting of two Ir atoms per catalytic site on the α -Fe₂O₃ substrate. The resulting catalysts preserve the atomic arrangements of the active two metal centers (Ir–O–Ir) but present two key features. First, the Ir DHCs are tightly bound to the supporting substrate (α -Fe₂O₃) and show outstanding stability against aggregation or detachment. Second, the catalysts are highly active toward water oxidation even without the organic ligands, which are critical to the functionality of the homogeneous analog (18). Significantly better performance than Ir SACs or Ir NPs was measured on Ir DHCs.

Results

Synthesis Strategy for Ir DHCs. Building upon our previous successes in immobilizing homogeneous water oxidation catalysts (Ir homodimer) (19), we designed the synthesis of Ir DHCs as shown in Fig. 1. The key step added to this work is the photochemical treatment, which was implemented to remove the organic ligands. The characterization of the α -Fe₂O₃ substrate and the resulting catalysts at each stage are presented in *SI Appendix*, Figs. S1–S3. In addition to structure results to be presented below, X-ray photoelectron spectroscopy (XPS) (*SI Appendix*, Fig. S2) and electron energy-loss spectroscopy (EELS) (*SI Appendix*, Fig. S3) clearly support that there is no N signal after the photochemical treatment. This provides strong evidence that the pyridyl ligands in the precursor have been removed.

Direct Structure Characterization of Ir DHCs. The most direct evidence that proves we have obtained a dinuclear structure of Ir atoms that are not in direct contact but connected by an oxygen bridge is from the high-angle annular dark-field scanning transmission electron microscopy (HAADF-STEM) data (Fig. 2*A* and *B* and *SI Appendix*, Figs. S4–S11). The bright two-point features in Fig. 2*A* were identified as Ir DHCs, and the lighter gray points in the background were ascribed to Fe atoms. Tilting experiments confirmed that the Ir atoms are on top of the Fe columns (*SI Appendix*, Fig. S7). Nevertheless, we caution that we could not fully rule out the existence of other species not aligned with the Fe columns by STEM characterization alone. Spectroscopic evidence lent additional support on this front (*vide infra*). The ultrahigh signal-to-noise ratio was enabled by the high-Z contrast of Ir and Fe. Importantly, few other components, such as Ir SACs or Ir NPs, were observed within the viewing field (more discussions on the distribution in *SI Appendix*, Fig. S12), which is critical to this work because the SACs and NPs would otherwise complicate the mechanistic understanding of water oxidation by Ir DHCs. To

further study the atomic arrangement of the Ir DHCs, a linescan for HAADF intensity was taken across the bright spots (Fig. 2*B*), and the intensity data are plotted in Fig. 2*C*. The average distance between the two Ir atoms within a DHC was measured at ~ 3 Å. Elemental mapping using STEM–energy-dispersive X-ray spectroscopy (EDS) (Fig. 2*D–G* and *SI Appendix*, Fig. S4) further supported that there were no large aggregates of Ir clusters. The lack of Ir SACs or clusters was proven by spectroscopic characterization to be discussed below. Taken as a whole, the unique two-atom arrangement and the lack of aggregated byproducts set the stage for detailed studies of DHCs as a new class of water-oxidation catalyst.

Our previous work has proven that the Ir–O–Ir arrangement within the Ir homodimer (Fig. 1) is key to its high activity toward water oxidation (18, 19). We therefore expect that Ir–O–Ir rather than Ir–Ir arrangement is preserved in the Ir DHC. Evidence from at least two complementary experimental techniques strongly supports our expectation. First, we performed in situ CO diffuse reflectance infrared Fourier transform (DRIFT) spectroscopic characterization, and the purpose was to use CO as a probe to study the Ir atomic arrangement within the DHC. While the dinuclear nature of the structure is unambiguously confirmed by the HAADF data, an alternative arrangement to the proposed one could feature Ir–Ir bonding. In the in situ CO DRIFT experiment, the two arrangements are expected to be readily distinguished by the characteristic absorption features at $\sim 1,850$ cm^{−1}, which is indicative of the bridge adsorption of CO at the Ir–Ir site (20). Indeed, the broad peak at $\sim 1,850$ cm^{−1} was observed for Ir NPs control samples with known Ir–Ir bonding (Fig. 2*I*) but absent from Ir DHCs (Fig. 2*H*). Additionally, a strong dipole–dipole coupling effect between adjacent CO probe molecules was evident in the control sample with Ir aggregates but was absent in Ir DHCs, further confirming the atomic dispersity of the latter. When the oxygen bridge of Ir DHC was broken to yield Ir SAC, we observed a redshift of the peaks characteristic of dicarbonyl species (*SI Appendix*, Fig. S13). Second, X-ray absorption spectroscopy data were acquired to reveal the coordination environment of the Ir center. We see from *SI Appendix*, Figs. S14–S16 and Table S1 that the first shell coordination of Ir in DHCs is dominated by Ir–O (21), in excellent agreement with the proposed bonding of Ir–O–Ir but not Ir–Ir. Taken together, the microscopic and spectroscopic characterization unambiguously confirmed that we have obtained a dinuclear Ir catalyst that features discrete Ir–O–Ir rather than Ir–Ir structures without organic ligands. Here we further highlight the uniqueness of the synthesis method. Our previous experiments show that other treatments such as thermal annealing (19) or electrochemical decomposition (22) lead to obvious Ir aggregation. Only by photochemical treatments could we achieve the DHC structure in the high yield (>80%).

Determination of Binding Sites by Density-Functional Theory and HAADF Simulation. The strong metal–support interaction is crucial to maintaining the catalytic structure under catalytic operation conditions for many systems (4). How SACs can be anchored onto supporting substrates by defect sites has been demonstrated on reducible metal oxides (23). Nevertheless, it would be a significant challenge to rely on the randomly distributed defect sites as the binding sites for DHCs that feature well-defined and uniform M–O–M arrangements. To understand how our Ir DHCs bind to the α -Fe₂O₃ support, we carried out density-functional theory (DFT) calculations. Our strategy was to construct hydroxyl-terminated α -Fe₂O₃ (001) surfaces, as shown

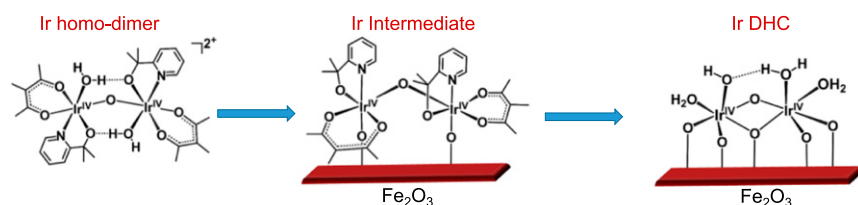


Fig. 1. Synthesis procedure of Ir DHC. It starts with the immobilization of molecular Ir catalysts, followed by photochemical removal of organic ligands. The binding details of H₂O and OH groups are proposed.

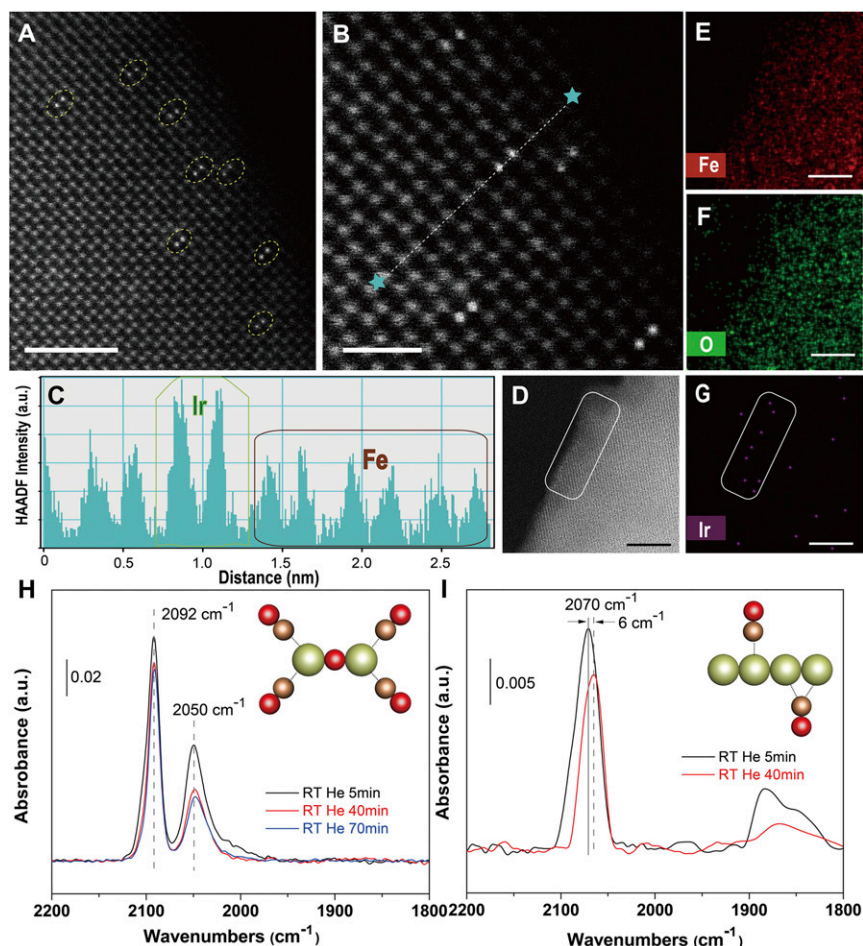


Fig. 2. Direct structural characterization of Ir DHC on α -Fe₂O₃. (A and B) Representative HAADF-STEM micrographs along [241] zone axis, in which the bright pairs are ascribed to Ir DHCs. The dotted line between the two stars in B represents the linescan for HAADF intensity analysis as shown in C. (D) Dark-field image of the region (outlined by white window) mapped in E–G for the distribution of Fe, O, and Ir, respectively. [Scale bars: (A) 2 nm; (B) 1 nm; (D–G): 4 nm.] (H and I) In situ DRIFT spectra of Ir DHCs (H) and NPs (I) in He flow 5 (black), 40 (red), and 70 (blue) min after CO adsorption at room temperature. The schematic atomic arrangement of the structures corresponding to the spectra are shown as insets. Green ball is Ir, red ball is O, and brown ball is C.

in Fig. 3A. Previous studies have shown that hydroxyl termination is the most stable in the presence of gas-phase H₂O (24). The optimized surface structures suggested that the Ir–O–Ir structure is stabilized by substrate O, H₂O, and –OH ligands (Fig. 3C and D). Taken together, the two Ir atoms in the resulting DHC are bound by five surface O atoms, each Ir atom occupying a threefold hollow site on the OH-terminated α -Fe₂O₃ surface (*SI Appendix*, Fig. S18). Importantly, the model built here allowed us to simulate the expected HAADF image under the experimental condition (Fig. 3E), which is in excellent agreement with the experimental data in terms of the Ir atomic location (Fig. 3A). Similarly, the simulated intensity linescan data reproduced the experimental ones as well, illustrating the accuracy of the interatomic distance in Ir–O–Ir site (Fig. 3B and F). We note that the data presented here represent a typical example of one facet of α -Fe₂O₃ (001), which provides a basis for more comprehensive future studies of other facets.

Catalytic Characterization of Ir DHCs. Photoelectrochemical (PEC) characterization was next carried out to study the catalytic activity of the Ir DHC following previously developed protocols. The Ir-based catalysts are known to be most active under acidic conditions (19). As such, it is desirable to study them at low pHs. The support (α -Fe₂O₃), however, would be dissolved by acids, leading to possible detachment of Ir that would undermine efforts to study its inherent catalytic activity and stability. For these reasons, we optimized the test conditions at a pH of 6.0. As shown in Fig. 4A, compared with control samples with only α -Fe₂O₃ support (bare in Fig. 4A), the addition of Ir catalysts improved the overall performance by shifting the polarization curves toward the cathodic direction. Previous thermodynamic and kinetic studies

have revealed that such a shift may be due to either improved charge separation within the support or better charge-transfer kinetics or a combination of both (25, 26). Given that the surface coverage of Ir DHCs on α -Fe₂O₃ is sparse, we strongly believe faster kinetics is the true reason for such a shift. The understanding is consistent with our previous kinetic studies (25). The per-atom turnover frequency (TOF) of Ir DHCs at 1.23 V (vs. reversible hydrogen electrode, RHE) is 2.6 and 5 times higher than the corresponding Ir SACs (*SI Appendix*, Fig. S20) and Ir NPs (*SI Appendix*, Fig. S21), respectively, at the same potential. In addition, compared with similar systems that feature Ir-based water photo-oxidation reactions (22, 25, 27–29), the Ir DHC on α -Fe₂O₃ features the higher normalized TOFs (*SI Appendix*, Table S3). That the sample with Ir DHCs exhibited the high activity attests to its functionality as an effective water-oxidation catalyst despite the fact that the organic ligands of the molecular precursor have been removed.

Proposed Catalytic Mechanism by DFT Calculations. Inspired by our previous studies on the Ir homogeneous catalysts (18) (*SI Appendix*, Fig. S22), we propose a mechanism that involves multiple proton-coupled electron transfer (PCET) steps by DFT calculations using the model built in Fig. 3C and D. Ir DHCs and homodimer molecules (18) share similar Ir^{IV}(OH₂)–O–Ir^{IV}(OH₂) structural motifs ($x = 2$ for Ir homodimer and $x = 1$ for Ir DHCs). Thus, it is reasonable to assume that the water-oxidation mechanism of Ir DHCs is similar to their homogeneous molecular analogs, albeit in the absence of the organic supporting ligands. As shown in Fig. 5A, Ir DHCs are proposed to undergo three PCET processes to build enough oxidation potential to oxidize H₂O and produce Ir–OOH (steps E to F). The free-energy changes of the

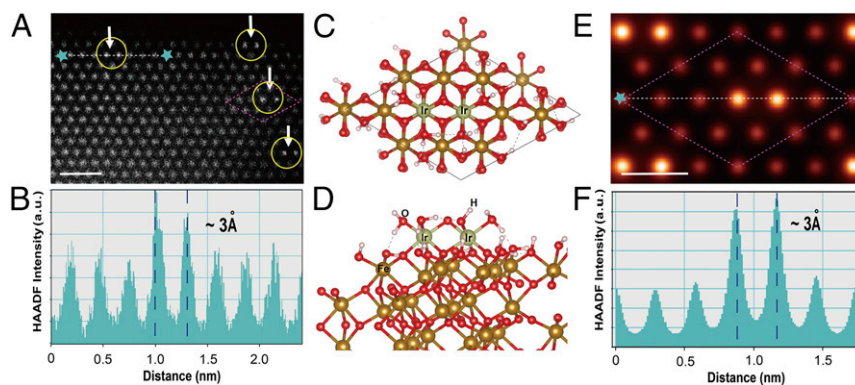


Fig. 3. Binding sites of Ir DHC on α -Fe₂O₃. Atomic resolution experimental (A) and simulated (E) HAADF-STEM micrographs of Ir DHC. The basis for the HAADF-STEM simulation is the atomic structure as shown in C and D. (Scale bars: A, 1 nm, E, 0.5 nm.) Proposed atomic structure of Ir DHC (support: α -Fe₂O₃). Top view along [001] zone axis (C) and side view (D). In the atomic model, green ball is Ir, gold ball is Fe, red ball is O, and white ball is H. The corresponding experimental (B) and simulated (F) HAADF line-intensity profiles show excellent match.

three PCET steps are 1.06, 1.37, and 1.21 eV, respectively, at $U = 0$ V (U is the applied potential; Fig. 5A). A substrate H₂O molecule binds to the Ir DHC with a free-energy increase of 0.44 eV, which then undergoes nucleophilic attack to form hydrogen peroxide with a free-energy increase of 0.36 eV. The oxidation of Ir-OOH intermediate F is easy to proceed through a PCET, requiring only 0.75 eV. The subsequent O₂ release is driven by the following substrate H₂O binding. By comparing the free-energy changes under different applied potentials, an overpotential as low as 0.14 V is enough for the overall four-electron oxidation to be thermodynamically downhill. The calculated overpotential indicates that the Ir DHC is an efficient catalyst for water oxidation, consistent with the experimentally observed low onset potential of the Ir DHC/ α -Fe₂O₃ ($V_{on} = 0.55$ V, corresponding to an applied potential of ~ 1.35 V by assuming a photovoltage of 0.8 V by α -Fe₂O₃) (26).

As an important control experiment, we carried out DFT calculations to compare the catalytic steps between the Ir DHC and SAC (Fig. 5 and *SI Appendix*, Figs. S23 and S24). The atomic structure of Ir SAC was built by placing one Ir atom in one threefold O site. The resting state of Ir SAC was identified as an Ir (IV) bound with an OH⁻ and two H₂O ligands (Fig. 5B). For water oxidation, Ir SAC first undergoes PCET processes twice, which is similar to the first two steps of water oxidation by Ir DHC. The key difference between the two catalysts lies in the next step. Whereas Ir DHC undergoes another PCET (steps C to D in Fig. 5A) before forming the O–O bond, Ir SAC has to bind to a H₂O substrate and form the O–O bond first (steps C to E in Fig. 5B) before the third PCET. This is because direct oxidation of Ir SAC after the second PCET step would require too high an energy (more than 1.8 eV). By comparison, the availability of another Ir atom nearby in Ir DHC reduces the energy need to

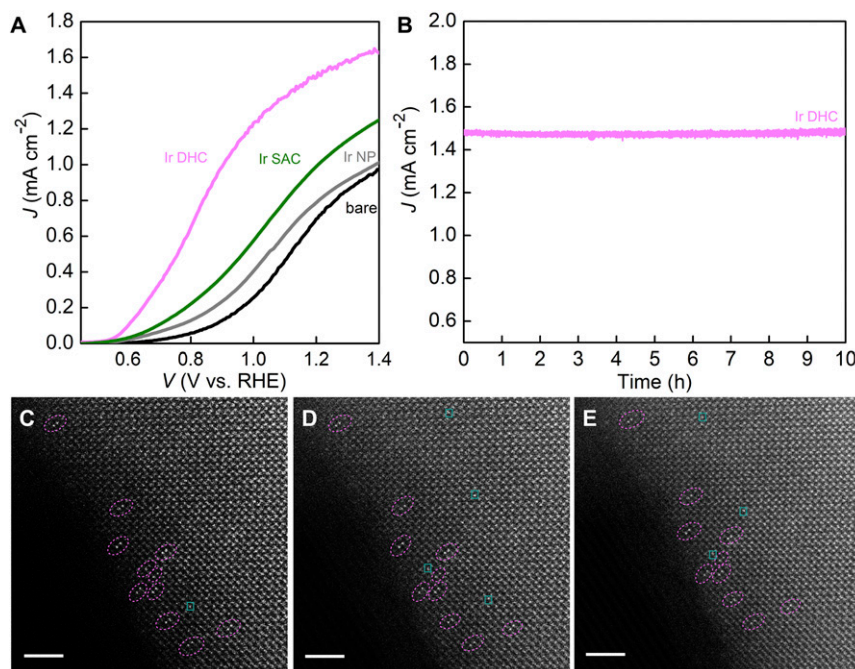


Fig. 4. Catalytic performance of Ir DHC in water photooxidation. (A) The polarization curve of the Ir DHC (pink) in comparison with three control samples, the Ir SAC (green), Ir NP (gray), and bare α -Fe₂O₃ support (black). The electrolyte was 0.1 M KNO₃ (pH 6.0), and the illumination intensity was 100 mW cm⁻² with AM 1.5 filters. (B) Chronoamperometry showing the stability of Ir DHC over 10 h with negligible decay. Evolution of Ir DHC on α -Fe₂O₃ during electron beam exposure for the following times: (C) 0 s, (D) 35 s, (E) 75 s. The electron dose received by the sample was ~ 100 eV/Å²/s. (Scale bar: 2 nm.)

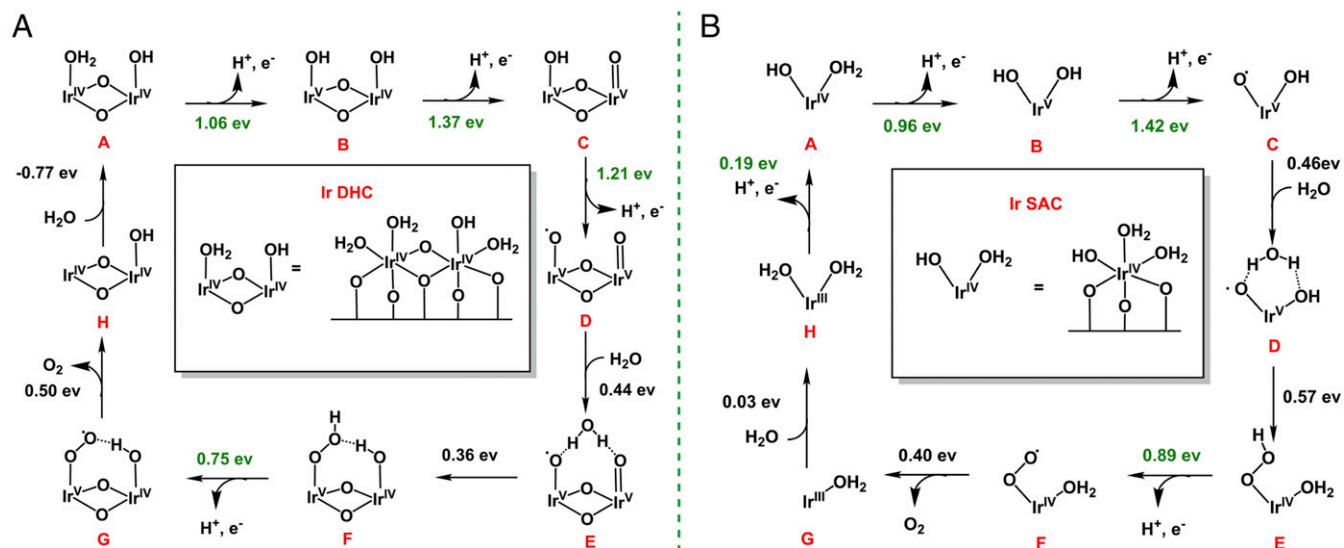


Fig. 5. Reaction mechanisms. Proposed reaction pathway and DFT calculated reactions free energies at zero bias potential ($U = 0$ V) of Ir DHC (A) and Ir SAC (B). Reaction free energies in green correspond to proton-coupled electron transfer steps which could be driven by applying bias potentials.

1.2 eV. We note that more accurate calculations of the energy need for catalytic steps would require the inclusion of the supporting substrate ($\alpha\text{-Fe}_2\text{O}_3$) and solvation effects, which is beyond the scope of the present work. Our results nonetheless highlight the benefits of the synergistic effects between a dinuclear catalytic site (Ir DHC) over a mononuclear site (Ir SAC). The understanding aligns with recent experiment observations that a dinuclear site may be more active toward water oxidation (30, 31). We emphasize that the well-defined structure of the Ir DHC is key to our understanding reported here, which permits the construction of mechanistic models for detailed studies of the processes.

Stability Characterization of Ir DHCs. We characterized the stability of Ir DHCs in two different settings. First, the chronoamperometry data of Ir DHCs on $\alpha\text{-Fe}_2\text{O}_3$ for the first 10 h were compared with other Ir catalysts. No measurable degradation was observed (Fig. 4B), suggesting that under PEC conditions the Ir DHC on $\alpha\text{-Fe}_2\text{O}_3$ is stable. The stability is better than Ir SACs and Ir NPs (SI Appendix, Fig. S25). Inductively coupled plasma optical emission spectroscopy (ICP-OES) characterization indicated that no Ir was detected in the electrolytes of the Ir DHCs. In addition, the key features in the data of STEM-EDS, in situ DRIFTS, and XPS by Ir DHCs after PEC test are similar to those by fresh samples, indicating that there was no aggregation (SI Appendix, Figs. S26–S28). Second, the Ir DHCs were subjected to focused electron beam irradiation under HAADF-STEM conditions; the purpose was to observe the inherent thermal stability of Ir DHCs. As seen in Fig. 4 C–E, no aggregation or detachment was observed for up to ~ 1 min of irradiation, which is longer than the reported SAC systems under the similar condition (32). The O_3 -binding site offered by the $\alpha\text{-Fe}_2\text{O}_3$ substrate has proven critical to the formation and stability of Ir DHCs (Fig. 3 C and D and SI Appendix, Fig. S18). We envision, however, that the binding is not unique to the chemical nature of the $\alpha\text{-Fe}_2\text{O}_3$ substrate. As long as similar binding sites are available, Ir DHC structures with comparable stabilities and catalytic activities are expected on other supporting substrates.

Conclusion

Heterogeneous catalysts with active moieties that are well defined in their atomic and/or molecular structures are expected to play important roles in the development of catalysis. The main challenge of this research direction lies in the synthesis and characterization of such catalysts. Within this context, the Ir DHCs reported here represent a significant advance. Not only are Ir DHCs a heterogeneous catalyst featuring two active-metal atoms,

their structures are also well characterized at the atomic level. The atomic arrangement of the catalytic center (Ir–O–Ir), which is key to the water-oxidation activities, is preserved by the strong binding provided by the supporting substrate. The resulting Ir DHC exhibits outstanding stability against aggregation or detachment. It shows high activity toward water oxidation. The finding is built upon recent advances aimed at synthesizing and studying SACs but takes a crucial step forward. It presents opportunities to study the detailed mechanisms of heterogeneous catalysis involving multiple but individually separated active atoms, which was carried out using DFT in this article. The insights are expected to contribute to the design and optimization of heterogeneous catalysts and electrocatalysts.

Materials and Methods

Preparation of Ir Dinuclear Catalyst on $\alpha\text{-Fe}_2\text{O}_3$ (Ir DHC) and Loading Estimate.

Step 1. An $\alpha\text{-Fe}_2\text{O}_3$ substrate was soaked in the Ir homodimer solution for 10 h and then thoroughly rinsed with deionized water to form the Ir intermediate. The loading amount was estimated by comparing the change of the UV-vis absorbance of the Ir homodimer solution. We used the average absorbance decrease for a 32-time loading procedure, the overall geometry area being ~ 94.4 cm^2 . The Ir loading was calculated to be $\sim 30\text{--}36$ nmol/cm^2 , which was confirmed by ICP-OES measurements.

Step 2. The photochemical treatments were conducted using a UVO cleaner system (Jelight Company Inc.) equipped with a UV light. In a typical procedure, the Ir intermediate sample was placed in the middle of the UVO chamber. The process lasted 28 min to get Ir DHCs.

Preparation of Ir Single-Atom Catalysts on $\alpha\text{-Fe}_2\text{O}_3$ (Ir SAC).

Similar to the preparation of Ir DHC, Ir SAC was obtained by carrying out step 2, the photochemical treatments for 40 min. The loading of Ir SAC is the same as the loading of Ir DHC sample, because no Ir evaporates during the photochemical treatment.

Preparation of Ir-Based Nanoparticles on $\alpha\text{-Fe}_2\text{O}_3$ (Ir NP).

Method 1. As-prepared Ir intermediate/ $\alpha\text{-Fe}_2\text{O}_3$ was annealed at 550 $^\circ\text{C}$ under Ar atmosphere for 30 min to form Ir NPs/ $\alpha\text{-Fe}_2\text{O}_3$.

Method 2. Ir intermediate/ $\alpha\text{-Fe}_2\text{O}_3$ was placed in the middle of the UVO generator chamber for 60 min under UV-ozone conditions.

STEM. All samples were scraped from the F-doped tin oxide electrode and collected on Lacey carbon grids. HAADF-STEM images (Fig. 2 D–G and SI Appendix, Fig. S1) were collected using a double-aberration-corrected FEI Titan3 G² 60–300 instrument operating at 300 kV. The semiangle of the probe-forming aperture was ~ 22 mrad. The inner and outer semiangles of the HAADF detector were ~ 80 and 200 mrad, respectively. A probe current of 76 pA and dwelling

time of 16 μs per pixel were chosen for desirable signal-to-noise ratios. EDS was performed on a Super-X EDS system consisting of four Bruker silicon drift detectors. During EDS mapping, sample drifting was corrected by a simultaneous image collector. The Fe K edge, O K edge, and Ir M edge were used for elemental mapping. EELS were collected with a GIF quantum EELS spectrometer; a standard power-law background subtraction was utilized to remove the background. Figs. 2 A and B, 3A, and 4 C–E and *SI Appendix, Figs. S4–S6 and S9* were collected on an FEI Titan G2 80–200 Crewley “ChemiSTEM” microscope, which was equipped with a high-brightness field-emission gun, a probe spherical aberration (Cs) corrector, and a super-X EDS system (33). The semiconvergence angle for imaging was ~ 24.7 mrad, while the collection semiangle was ~ 70 –200 mrad. A higher beam current of 280 pA was used with a longer dwell time of 0.1 ms per pixel and repeated 200 \times for atomic-resolution EDXS mapping. Spatial drifting was corrected using a simultaneous image collector. All high-resolution HAADF images shown in this work are raw data without any postfiltering.

In Situ DRIFTS. In situ DRIFTS measurements were performed using a Nicolet i550 FTIR spectrometer equipped with a DTGS KBr detector and a Harrick praying mantis HVC-DRP4 cell equipped with KBr windows (34). After each sample was placed in the cell, it was heated to 105 $^{\circ}\text{C}$ under pure He for at least 15 min to remove physically adsorbed H_2O and was then gradually cooled to room temperature. Ir NPs/ $\alpha\text{-Fe}_2\text{O}_3$ prepared by method 1 was further treated under 20% H_2 at 150 $^{\circ}\text{C}$ for 2 h to remove potential thin oxide surface coatings. Background spectra were then recorded at room temperature. Subsequently, the gas flow was changed to CO for 15 min and was changed back to He to avoid possible interference of gaseous CO to the spectra. DRIFT spectra were recorded in the CO absorption region, 2,200–1,800 cm^{-1} after varying the He purging time (5, 10, 40, and 70 min). The resolution was selected at 4 cm^{-1} . Sixty-four scans were recorded for each spectrum shown in the work.

PEC Characterization. PEC measurements were carried out using a potentiostat (Modulab XM equipped with Modulab XM ECS software). The light source was a solar simulator (100 mW/cm^2 , Solarlight model 16S-300-M Air Mass Solar Simulator, AM 1.5). Ir DHC/ $\alpha\text{-Fe}_2\text{O}_3$, Ir SAC/ $\alpha\text{-Fe}_2\text{O}_3$, Ir NPs/ $\alpha\text{-Fe}_2\text{O}_3$, and $\alpha\text{-Fe}_2\text{O}_3$ were used as the working electrodes, with an SCE electrode as the reference electrode, and a Pt wire used as the counterelectrode. The electrolyte was a

0.1 M KNO_3 solution with the pH adjusted to 6.0. The potential was corrected to the RHE scale by the Nernst equation ($E_{\text{RHE}} = E_{\text{SCE}} + 0.059 \text{ pH} + 0.241$). For linear sweep voltammetry data, the scan rate was 20 mV/s .

Computational Details. We used the Vienna ab initio simulation package (VASP) for all periodic boundary calculations (35). Projector augmented plane-wave method (36) together with the Perdew–Burke–Ernzerhof exchange–correlation functional (37) were employed to describe the electron–ion interactions. A cutoff of 450 eV was chosen for the plane-wave basis set in all calculations. A $5 \times 5 \times 5$ Monkhorst–Pack-type k -point grid was chosen for the optimization of bulk Fe_2O_3 . The Gaussian smear method was used for Fe_2O_3 . The σ value was chosen to be 0.1 eV. The energy convergence criterion was set to be 10^{-4} eV per unit cell and the geometry convergence criterion was set to be 10^{-3} eV per unit cell for energy difference between two consecutive ionic steps. Additional details of the calculations are available in *SI Appendix*.

ACKNOWLEDGMENTS. We thank Dr. Xiahui Yao for support during the acquisition of XPS data and helping draw the schematic figure, and Wei Li and Da He for assistance with PEC data analysis. We thank Dr. Stafford W. Sheehan and Dr. Song Li for discussions. We also thank Dongsheng Song and Shucheng Yu for STEM data analysis discussions. X.Y. and X.P. thank the support of the University of California, Irvine Materials Research Institute for the use of TEM facilities. Work done at Boston College was in part supported by the National Science Foundation (DMR 1055762) for materials synthesis and photoelectrochemical studies; precursor synthesis and theoretical computations at Yale University were supported by the Argonne-Northwestern Solar Energy Research Center, an Energy Frontier Research Center funded by the US Department of Energy (DOE), Office of Science, Office of Basic Energy Sciences (BES), under Award DE-SC0001059. HAADF-STEM work was supported by the National Key Research and Development Program (2016YFB0700402), DOE, BES, Division of Materials Science and Engineering, under Grant DE-SC0014430, the National Basic Research Program of China (Grant 2015CB654901), the National Natural Science Foundation of China (11474147), the Natural Science Foundation of Jiangsu Province (Grant BK20151383), and the Fundamental Research Funds for the Central Universities (021314380077). In situ DRIFTS studies are supported by the DOE under Award DE-FG02-05ER15730. The Advanced Light Source is supported by the Director, Office of Science, DOE, BES, under Contract DE-AC02-05CH11231.

1. Fu Q, Saltsburg H, Flytzani-Stephanopoulos M (2003) Active nonmetallic Au and Pt species on ceria-based water-gas shift catalysts. *Science* 301:935–938.
2. Liu J, et al. (2016) Tackling CO poisoning with single-atom alloy catalysts. *J Am Chem Soc* 138:6396–6399.
3. Kyriakou G, et al. (2012) Isolated metal atom geometries as a strategy for selective heterogeneous hydrogenations. *Science* 335:1209–1212.
4. Flytzani-Stephanopoulos M, Gates BC (2012) Atomically dispersed supported metal catalysts. *Annu Rev Chem Biomol Eng* 3:545–574.
5. Liu P, et al. (2016) Photochemical route for synthesizing atomically dispersed palladium catalysts. *Science* 352:797–801.
6. Jones J, et al. (2016) Thermally stable single-atom platinum-on-ceria catalysts via atom trapping. *Science* 353:150–154.
7. Asakura K, Kitamura-Bando K, Iwasawa Y, Arakawa H, Isobe K (1990) Metal-assisted hydroformylation on a SiO_2 -attached rhodium dimer. In situ EXAFS and FT-IR observations of the dynamic behaviors of the dimer site. *J Am Chem Soc* 112:9096–9104.
8. Yang D, Xu P, Browning ND, Gates BC (2016) Tracking Rh atoms in zeolite HY: First steps of metal cluster formation and influence of metal nuclearity on catalysis of ethylene hydrogenation and ethylene dimerization. *J Phys Chem Lett* 7:2537–2543.
9. Yang D, Xu P, Guan E, Browning ND, Gates BC (2016) Rhodium pair-sites on magnesium oxide: Synthesis, characterization, and catalysis of ethylene hydrogenation. *J Catal* 338:12–20.
10. Sushkevich VL, Palagin D, Ranocchiari M, van Bokhoven JA (2017) Selective anaerobic oxidation of methane enables direct synthesis of methanol. *Science* 356:523–527.
11. Shan J, et al. (2014) Conversion of methane to methanol with a bent mono(μ -oxo) dinickel anchored on the internal surfaces of micropores. *Langmuir* 30:8558–8569.
12. Blakemore JD, Crabtree RH, Brudvig GW (2015) Molecular catalysts for water oxidation. *Chem Rev* 115:12974–13005.
13. Zhang B, et al. (2016) Homogeneously dispersed multimetal oxygen-evolving catalysts. *Science* 352:333–337.
14. Zandi O, Hamann TW (2016) Determination of photoelectrochemical water oxidation intermediates on hematite electrode surfaces using operando infrared spectroscopy. *Nat Chem* 8:778–783.
15. Brodsky CN, et al. (2017) In situ characterization of cofacial Co(IV) centers in Co_4O_4 cubane: Modeling the high-valent active site in oxygen-evolving catalysts. *Proc Natl Acad Sci USA* 114:3855–3860.
16. De Wolf S, Descoedres A, Holman Zachary C, Ballif C (2012) High-efficiency silicon heterojunction solar cells: A review. *Green* 2:7–24.
17. Young KJ, et al. (2012) Light-driven water oxidation for solar fuels. *Coord Chem Rev* 256:2503–2520.
18. Yang KR, et al. (2016) Solution structures of highly active molecular Ir water-oxidation catalysts from density functional theory combined with high-energy X-ray scattering and EXAFS spectroscopy. *J Am Chem Soc* 138:5511–5514.
19. Sheehan SW, et al. (2015) A molecular catalyst for water oxidation that binds to metal oxide surfaces. *Nat Commun* 6:6469.
20. Yamamoto H, et al. (2017) Monodisperse iridium clusters protected by phenylacetylene: Implication for size-dependent evolution of binding sites. *J Phys Chem C* 121:10936–10941.
21. Muratsugu S, et al. (2012) Surface-assisted transfer hydrogenation catalysis on a $\gamma\text{-Al}_2\text{O}_3$ -supported Ir dimer. *Phys Chem Chem Phys* 14:16023–16031.
22. Li W, et al. (2015) Hematite-based solar water splitting in acidic solutions: Functionalization by mono- and multilayers of iridium oxygen-evolution catalysts. *Angew Chem Int Ed Engl* 54:11428–11432.
23. Kwak JH, et al. (2009) Coordinatively unsaturated Al^{3+} centers as binding sites for active catalyst phases of platinum on $\gamma\text{-Al}_2\text{O}_3$. *Science* 325:1670–1673.
24. Trainor TP, et al. (2004) Structure and reactivity of the hydrated hematite (0 0 1) surface. *Surf Sci* 573:204–224.
25. Li W, et al. (2016) Comparison of heterogenized molecular and heterogeneous oxide catalysts for photoelectrochemical water oxidation. *Energy Environ Sci* 9:1794–1802.
26. Jang JW, et al. (2015) Enabling unassisted solar water splitting by iron oxide and silicon. *Nat Commun* 6:7447.
27. Moir JW, Sackville EV, Hintermaier U, Ozin GA (2016) Kinetics versus charge separation: Improving the activity of stoichiometric and non-stoichiometric hematite photoanodes using a molecular iridium water oxidation catalyst. *J Phys Chem C* 120:12999–13012.
28. Tilley SD, Cornuz M, Sivula K, Grätzel M (2010) Light-induced water splitting with hematite: Improved nanostructure and iridium oxide catalysis. *Angew Chem Int Ed Engl* 49:6405–6408.
29. Badia-Bou L, et al. (2013) Water oxidation at hematite photoelectrodes with an iridium-based catalyst. *J Phys Chem C* 117:3826–3833.
30. Ullman AM, Brodsky CN, Li N, Zheng S-L, Nocera DG (2016) Probing edge site reactivity of oxidic cobalt water oxidation catalysts. *J Am Chem Soc* 138:4229–4236.
31. Zhang M, de Respinis M, Frei H (2014) Time-resolved observations of water oxidation intermediates on a cobalt oxide nanoparticle catalyst. *Nat Chem* 6:362–367.
32. Aydin C, Lu J, Browning ND, Gates BC (2012) A “smart” catalyst: Sinter-resistant supported iridium clusters visualized with electron microscopy. *Angew Chem Int Ed Engl* 51:5929–5934.
33. Ernst Ruska-Center for Microscopy and Spectroscopy with Electrons (2016) FEI Titan G2 80-200 CREWLEY. *J Large-Scale Res Facil* 2:A43.
34. Lu J, Serna P, Aydin C, Browning ND, Gates BC (2011) Supported molecular iridium catalysts: Resolving effects of metal nuclearity and supports as ligands. *J Am Chem Soc* 133:16186–16195.
35. Kresse G, Furthmüller J (1996) Efficient iterative schemes for ab initio total-energy calculations using a plane-wave basis set. *Phys Rev B Condens Matter* 54:11169–11186.
36. Kresse G, Joubert D (1999) From ultrasoft pseudopotentials to the projector augmented-wave method. *Phys Rev B* 59:1758–1775.
37. Perdew JP, Burke K, Ernzerhof M (1996) Generalized gradient approximation made simple. *Phys Rev Lett* 77:3865–3868.